

<https://doi.org/10.1038/s42003-023-04788-0>

OPEN

Debiased ambient vibrations optical coherence elastography to profile cell, organoid and tissue mechanical properties

Jonathan H. Mason^{1,9}, Lu Luo^{2,9}, Yvonne Reinwald³, Matteo Taffetani⁴, Amelia Hallas-Potts^{1,5}, C. Simon Herrington¹, Vlastimil Srsen¹, Chih-Jen Lin¹, Inês A. Barroso⁷, Zhihua Zhang⁷, Zhibing Zhang⁷, Anita K. Ghag⁷, Ying Yang⁸, Sarah Waters⁴, Alicia J. El Haj² & Pierre O. Bagnaninchi¹

The role of the mechanical environment in defining tissue function, development and growth has been shown to be fundamental. Assessment of the changes in stiffness of tissue matrices at multiple scales has relied mostly on invasive and often specialist equipment such as AFM or mechanical testing devices poorly suited to the cell culture workflow. In this paper, we have developed a unbiased passive optical coherence elastography method, exploiting ambient vibrations in the sample that enables real-time noninvasive quantitative profiling of cells and tissues. We demonstrate a robust method that decouples optical scattering and mechanical properties by actively compensating for scattering associated noise bias and reducing variance. The efficiency for the method to retrieve ground truth is validated in silico and in vitro, and exemplified for key applications such as time course mechanical profiling of bone and cartilage spheroids, tissue engineering cancer models, tissue repair models and single cell. Our method is readily implementable with any commercial optical coherence tomography system without any hardware modifications, and thus offers a breakthrough in on-line tissue mechanical assessment of spatial mechanical properties for organoids, soft tissues and tissue engineering.

¹ MRC Centre for Regenerative Medicine, The University of Edinburgh, Edinburgh, UK. ² Healthcare Technology Institute, University of Birmingham, Birmingham, UK. ³ Department of Engineering, Nottingham Trent University, Nottingham, UK. ⁴ Mathematical Institute, University of Oxford, Oxford, UK. ⁵ Cancer Research UK Edinburgh Centre, The University of Edinburgh, Edinburgh, UK. ⁶ MRC Centre for Reproductive Health, The University of Edinburgh, Edinburgh, UK. ⁷ School of Chemical Engineering, University of Birmingham, Birmingham, UK. ⁸ Institute of Science and Technology in Medicine, Keele University, Stoke-on-Trent, UK. ⁹These authors contributed equally: Jonathan H. Mason, Lu Luo. [✉]email: a.elhaj@bham.ac.uk; pierre.bagnaninchi@ed.ac.uk

The mechanical environment in tissue homeostasis has been shown to be fundamental to multiple organ function, development and pathology^{1–3}. Matrix stiffness can be an informative indicator in many biological and medical applications. In tissue engineering, the bulk and spatial mechanical properties of engineered grafts is crucial to their clinical success after implantation^{4–7}. For example, nutrient limitation can create a softer central region in engineered cartilage^{8,9}. In cancer research, stiffness differentiates malignant tissue from healthy tissue¹⁰, and monitoring the change in stiffness of 3D cancer cell model in response to anti-cancer drug treatment may potentially indicate the effectiveness of the drug¹¹. In the eye, the stiffness of the cornea is indicative of its optical performance under intraocular pressure¹². Traditional approaches for testing the mechanical properties of engineered tissues usually requires direct contact with the tissue and are non-sterile, involving termination of the cell culture^{13,14}. Furthermore, it provides only bulk values rather than localised insight into the spatial mechanical heterogeneity of the engineered tissue. Manufacturing or long term cultures need easy continuous monitoring without damage to the 3D cultures and optical systems provide a potential solution. Therefore, a system is needed for sterile on line monitoring the bulk and spatial mechanical properties of in vitro 3D tissues such as cell seeded matrices, organoids or ex vivo explants.

The quantification and spatial mapping of stiffness, a process known as elastography, can be generally performed by stimulating a specimen, measuring its deformation, and inferring its mechanical properties through fitting to a parameterised model. Elastography was first implemented with ultrasound imaging¹⁵, then MRI¹⁶ and more recently with optical methods as recently reviewed¹⁷. Optical coherence tomography (OCT)¹⁸ is particularly well suited for elastography deformation tracking in small samples, due to its high-resolution non-invasive 3D imaging capacity¹⁹, and its ability to precisely encode displacement through its phase²⁰.

Early optical coherence elastography (OCE) methods used surface compression with speckle tracking^{21,22} and later phase lag measurement²³, but the concept has been realised with many other contact and non-contact forms of stimulation²⁴. One successful approach is to launch controlled shear waves in the material from point dynamic loading via an air-puff²⁵, and measure the spatially resolved wave velocity using OCT, which is closely tied to the material's stiffness²⁶, and has been demonstrated in vivo²⁷. Naturally occurring broadband diffuse shear waves can also be exploited to measure shear wavelength^{28,29}, a concept used by Nguyen et al.³⁰ with OCT where it is referred to as ‘passive elastography’. A closely related approach by Zvietcovich et al.³¹ measures shear wavelength from reverberant waves from an array of contact point sources vibrating at a single frequency, where it was successfully applied ex-vivo to quantifying corneal stiffness.

Passive elastography is a compelling technique for mechanical contrast, since it can be performed with OCT systems with no additional hardware modifications. Without need for contact with the materials, analysis can be done in a sterile manner for tissue engineering applications. Although the acquisition is both asynchronous and slow relative to the vibrating source, enabling the use of low frame sensors, one can still estimate the shear wavelength from a series of displacement fields using the cross-correlation Bessel fit algorithm of ref. ³¹ or displacement to strain energy ratio of ref. ³⁰. However, while the former has limited spatial resolution throughout the fitting plane, the latter is inherently biased by varying levels of noise. Therefore, we propose an analysis denoted debiased ambient vibrations OCE for forming a spatially variant debiased estimation of local wavelength, which is suitable for materials of different size and optical scattering properties.

Results

Robust passive elastography with noise debiasing. First we simulated a shear wave travelling in a biphasic material as per Eq. (4) (Fig. 1a) with a wavelength of $\lambda_1 = 2$ mm in the blue region and $\lambda_2 = 4$ mm in the yellow region, and tested the performance of our algorithm to retrieve the ground truth with a slow and asynchronous acquisition when compared to the vibrating source. Time-lapse phase measurements ($N=195$) corresponding to the displacement field induced by the shear wave travelling in the material (x - y plane) are simulated in Fig. 1b with an additive white Gaussian noise (variance $\sigma = 0.05$), and used as the inputs to the OCE algorithms estimating the wavelength along the x axis (Fig. 1c). The passive OCE algorithm as presented in ref. ³⁰ is biased by noise in the measurements, which we show theoretically. This effect is demonstrated in Fig. 1c, and further investigated with differing noise level variance in Fig. 1d. As the noise in displacement estimates from OCT is related to its signal-to-noise ratio^{32,33}, this passive elastography contrast is directly tied to the scattering properties of the material. Therefore, materials with identical stiffness but different optical scattering will be incorrectly differentiated with this algorithm. To alleviate this problem, we present an approach that actively compensates for this noise bias and reduces the variance through spatial filtering. The effectiveness of this are demonstrated in the wavelength maps in Fig. 1a and line profiles in Fig. 1c. The debiased estimate corrects for the average error, but introduces a large amount of variance, attributed to the bias-variance trade-off. Finally, our proposed debiased ambient vibration OCE algorithm produces a debiased low-variance estimate very close to the ground truth. Most importantly, the trends are consistent for varying noise levels in Fig. 1d, which allows the decoupling of scattering intensity and mechanical contrast.

Reliably measuring the elastic wavelength then allows one to produce an estimate of stiffness. For linearly elastic isotropic materials for example, $E \propto \lambda^2$, where E is the Young's modulus and λ is the wavelength estimated through our algorithm. Through calibration, and measurements under the same conditions, the constant of proportionality can be found. More details on the relationship between wavelength and elastic moduli are summarised below.

Validation with acellular agarose gel. We, then, validated our approach with acellular agarose gels of varying stiffness, which is summarised in Fig. 2, with implementation and processing details and experimental protocol fully described in ‘Methods’. After OCT imaging, the Young's modulus of these gels was measured using a standard compression test. The OCT intensity images and calculated mechanical contrast maps of these hydrogels are shown in Fig. 2a. All gels had the same amount of optical contrast agent but different concentration of agarose, shown to correlate with its stiffness³⁴, to decouple optical scattering and mechanical properties. There is a visible increase in stiffness estimate with increasing concentration from the λ -maps. Compared to the Young's modulus of groups of each gel concentration ($n = 3$), as shown in Fig. 2c, there is a strong linear correlation ($r = 0.994$) validating the model $E \propto \lambda^2$ for this material. We will henceforth refer to the mean wavelength squared, λ^2 , as ‘relative stiffness’.

The hybrid agarose shown in Fig. 2a shows the ability to measure heterogeneous stiffness and local variations, similar to that in ref. ³⁰. In this case, our algorithm produces a sharp contrast between the two halves of the gel and consistent with depth. Finally, we estimated the spatial resolution of our method and system from the edge transitions, with corresponding profile in Fig. 2b, to be 47.4 μm laterally and 38.1 μm axially, comparable to that reported by ref. ³¹; the method to calculate spatial

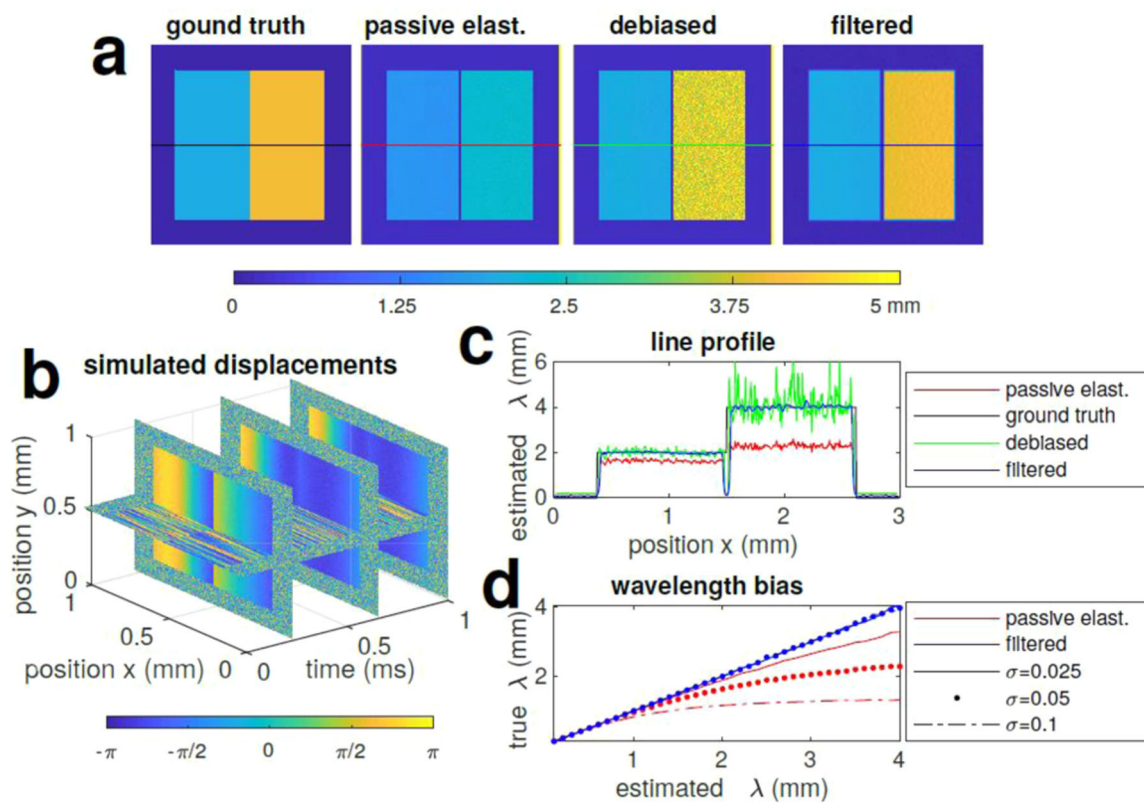


Fig. 1 Wavelength estimation from simulation. **a** Shows the ground truth with waves travelling laterally in a biphasic material at wavelength $\lambda_1 = 2$ mm and $\lambda_2 = 4$ mm, the biased estimation from passive elastography as per Eq. (6)²⁹, the high variance debiased estimate from Eq. (8) and the proposed debiased filtered estimate from Eq. (9), which forms the mechanical contrast. Wavelengths are colour coded in the figure as per colour bar. **b** Shows the simulated time-lapse phase measurement induced by the displacement field calculated from ground truth with the addition of a noisy background. **c** Shows the line profiles through the coloured regions in **a**. Panel **d** is the wavelength bias estimated for passive elastography (all red lines) and debiased ambient vibration OCE (blue lines) at increasing noise levels.

resolution is detailed in Methods section. Without debiasing, passive elastography can also provide similar mechanical contrast as shown in ref.³⁰. However the quantitative measurement of the shear wavelength is largely underestimated (see Figs. 1c and S2d) especially in the presence of noise (Fig. 1d). In contrast debiased ambient vibration OCE provide an accurate value for the wavelength in the simulation (Fig. 1c), even in the presence of noise (Fig. 1d), and a realistic value for the wavelength for real samples that correlates well with mechanical measurements (see Fig. 2c).

On line monitoring of mechanical properties of engineered bones and cartilage tissues. Matrix stiffness analysis during orthopaedic tissue engineering is critical to assessment and potentially outcome measures for manufacturing medical implants. As an application of debiased ambient vibration OCE analysis in bone tissue engineering, we cultured mesenchymal stem cell (MSC) pellets in osteogenic differentiation for 21 days, while continuously measuring their stiffness with debiased ambient vibration OCE in a sterile on line manner. Validation was conducted on a subset of sample with end-point mechanical testing. From mechanical testing, shown in Fig. 3b, there is a marked increase in the Young's modulus of engineered bone tissues throughout culture. This increase of mechanical contrast is also clear in the λ -maps in Fig. 3a in each of the pellets over time. The relative stiffness from debiased ambient vibration OCE was then quantified over each of the pellets and shown in Fig. 3c, showing a monotonic increase over culture for each sample, in line with the mechanical testing data. Increased staining for

collagen in osteogenic pellets was observed with culture time, indicating the growth in matrix content upon culture, further supporting the mechanical testing data and OCT analysis. Spatial heterogeneities were observed in both mechanical contrast maps and histology.

Then, we applied debiased ambient vibration OCE analysis to MSC cell pellets cultured in a chondrogenic medium for 21 days. $N=3$ samples were subjected to hydrostatic pressure to further enhance the differentiation, while the rest ($N=3$) were kept as control. As expected, biochemical analysis showed an increase in glycosaminoglycan (GAG) content in the stimulated group as shown in Fig. 3f, implying an increase in stiffness, and this is well reflected both in the λ -maps in Fig. 3e and quantitative analysis summarised in Fig. 3g.

Tissue engineered cancer model. We explored the potential of debiased ambient vibration OCE in cancer research for monitoring the spatial mechanical properties of a tissue engineered cancer model. We first cultured fibroblast seeded collagen gels for 11 days. As expected, our analysis showed a steady increase in the relative stiffness of the fibroblast seeded collagen gel upon culture time Fig. 4a, b. Then, ovarian cancer cells were seeded on top of the collagen gel for 7 days, and could easily be distinguished from the collagen gel layer by analysing the mechanical contrast between the two Fig. 4c, d. This was supported by histology (Fig. 4e, f).

Potential application for cornea repair. OCT is a routine tool for ophthalmology and our method could extend these capacities

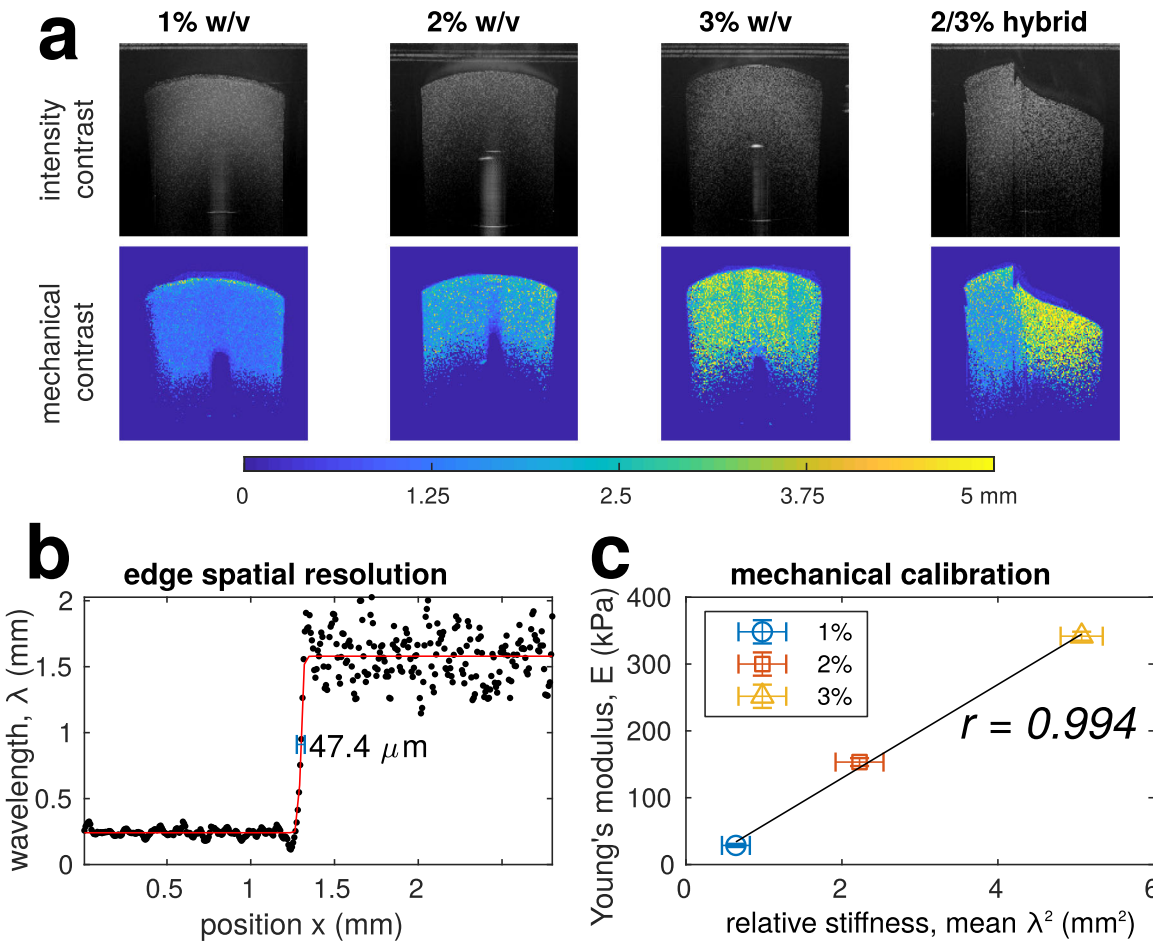


Fig. 2 Mechanical contrast and validation with differing concentration agarose gels with 1% w/v milk powder for optical contrast. **a** Shows examples of intensity and mechanical contrast. All pictures are 3×3 mm in size. Panel **b** is an edge line profile and spatial resolution as calculated as the FWHM of fitted sigmoid derivative as in Eq. (13); the corresponding axial edge spatial resolution was found to be 38.1 μm . **c** Mechanical calibration performed as a linear fit between squared wavelength and Young's modulus from Bose ElectroForce ($n=3$), assuming the elastic model in Eq. (3); error bars show the standard deviation. OCT intensity images are displayed as the logarithm of the mean intensity.

to routine monitoring of surface reconstructions. Thus, we investigated the potential of debiased ambient vibration OCE to assess the quality and efficiency of a gel system to repair small cornea lesions. Porcine corneas ($N=3$) were biopsy punched to generate a local wound. Then, a solution of 15% or 20% methacrylated silk fibroin solution was injected to the injury site, UV crosslinked and imaged with OCT (Fig. 5a). debiased ambient vibration OCE analysis showed a significantly higher relative stiffness in the 20% gel group, which is line with the mechanical data obtained by rheology testing (Fig. 5b, c). While OCT intensity images did not show any obvious voids at the interface between the gel and cornea in either group, clear voids were identified for both groups in the mechanical contrast (λ) map (see white arrows), indicating the existence of uncured gel solution. This suggests debiased ambient vibration OCE can be a powerful tool for assessing the quality and efficiency of tissue repair.

Potential application for oocyte screening. Routine fertility studies can involve assessment of the viability and developmental competence of pre-fertilised oocytes. Recent studies suggest the stiffness of oocyte is associated with its viability and embryo development potential³⁵. The application of the debiased ambient vibration OCE analysis to mouse oocytes is summarised in Fig. 5d. We compared intact and zona pellucida stripped oocytes from wild-type mice and Cabin1 knockout, which has been

shown to cause embryonic developmental arrest³⁶. Firstly, a significant difference in mean wavelength was observed against the control group, which could be a means to assess their viability as in refs. ^{35,37}. Mechanical contrast map showed a stiffer outer ring in wild type zona-intact when compared to zone-free and zona intact cabin1 knockout mice (Fig. 5d). This suggests that debiased ambient vibration OCE can be an effective tool for noncontact screening of developmentally competent oocytes in a noninvasive way, in contrast to micropipette aspiration³⁴.

Discussion

The debiased ambient vibration analysis is a postprocessing algorithm for deriving quantitative mechanical contrast maps from OCT scans, that decouples the scattering and mechanical properties. The approach is based upon the wavelength estimation of ambient elastic waves that are generated by multiple sources in laboratory conditions. In optical research laboratories, it is usually required to conduct experiments in a vibration-free environment. However, a host of close and distant sources of vibration such as heating, ventilation, air conditioning, incubators, pumps, computers, scientific equipment, road and rail transportation systems adds up into an unavoidable vibrational background noise that is coupled to the surrounding environment. To this end, optical systems are built on specialist passive or active vibration tables. However in our study we intentionally

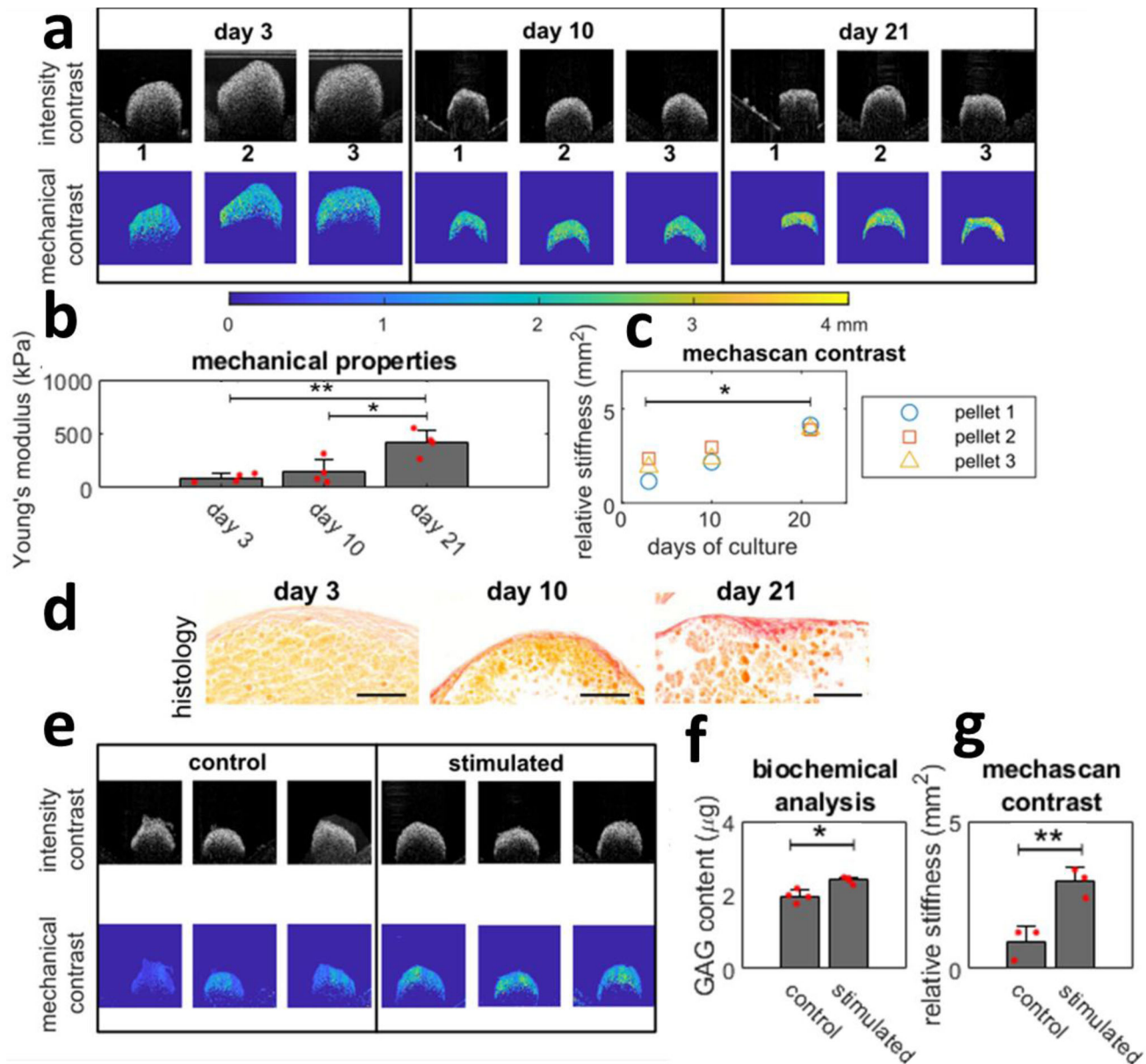


Fig. 3 On line monitoring mechanical properties of engineered bones and cartilage tissues. Panel **a** is examples of intensity and mechanical contrast of engineered bone tissues (in triplicate) on days 3, 10 and 21. All presented pictures are 1x1 mm. **b** Shows the Young's modulus of the tissue, tested by a customised compression rig ($n = 4$)⁴⁰. Panel **c** is relative stiffness for each sample throughout culture ($n = 3$). **d** Histology with picrosirius red staining for collagen content in osteogenic pellets at days 3, 10 and 21. Orange staining indicates cytoplasm and red staining indicates new synthesised collagen fibrils; scale bar: 100 µm. **e** Shows intensity and mechanical contrast of engineered cartilage tissues stimulated by hydrostatic pressure for 21 days. Panel **f** is glycosaminoglycans (GAG) content of samples ($n = 4$), and **g** shows relative stiffness from debiased ambient vibration OCE analysis ($n = 3$). * denotes a significant difference with a $p < 0.05$ and ** of $p < 0.01$ as calculated with 1-way Anova test followed by a Tukey-Kramer comparison of means. Error bars represent the standard deviation.

operate our OCT system on a bench to benefit fully from the ambient vibrations.

In addition we conducted FEM analysis to show that external vibrations applied to a well-plate do generate sufficient waves in the sample. It is also worth noting that in our experimental setup, we have to take steps to reduce the magnitude of environmental vibrations by placing the plate in a chamber with a rubber base to avoid phase wrapping and artifacts triggered by large displacements.

Ambient vibrations are also relevant for in vivo studies as naturally arising shear waves from human body activity were have been used to qualitatively assess the elastic properties of tissues^{28,38}.

In addition, the potential for in vivo passive optical coherence elastography has also been demonstrated for an anaesthetised eye rat cornea³⁰.

Spatial resolution is an important consideration for any imaging method, and the ability to resolve different material stiffness is a main advantage of OCE. Theoretically, our method is limited only by the number of pixels over which the strain power is calculated or the filter kernel. For the agarose study in Fig. 2, we calculate strain laterally with a sliding window of 7 pixels and use a Gaussian filter with spatial standard deviation of 5 pixels, leading to a FWHM of 11.8 pixels and expected spatial resolution of 41.3 µm laterally and 20.9 µm axially which is comparable to the 47.4 µm and 38.1 µm we measured empirically from the edge

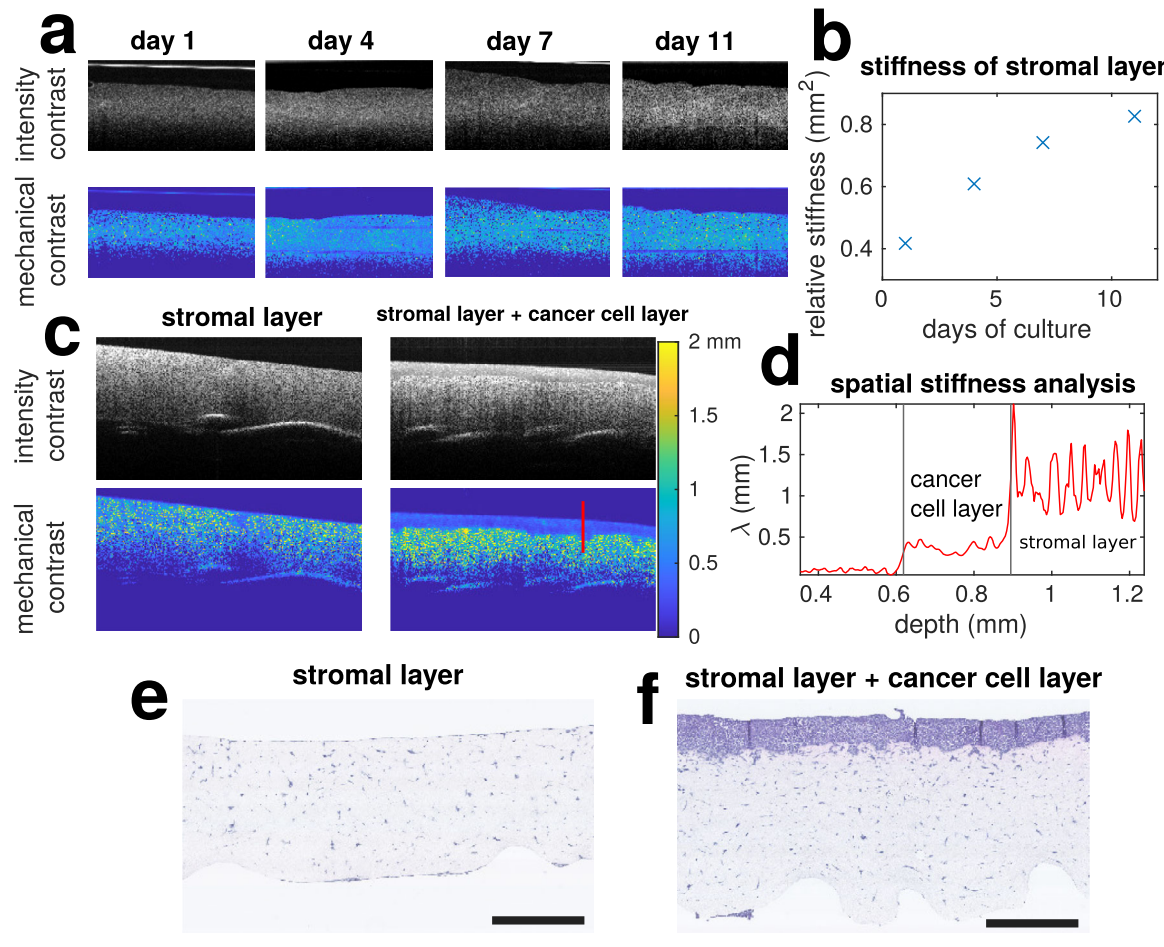


Fig. 4 On line mechanical measurement of a tissue engineered cancer model. **a** Shows the intensity and mechanical contrast of fibroblast seeded collagen gels over 11 day culture. All presented pictures are 6×3 mm. **b** Shows their corresponding stiffness over time. **c** Shows the intensity and mechanical contrast of collagen gels with and without cancer cell cultured on top for 7 days. **d** Mechanical properties measured along the red line displayed in **c**. **e**, **f** Histology images for **c** stained with haematoxylin and eosin. Scale bar: 1 mm.

transition. In the presence of noise, there is a trade-off between bias, spatial resolution and variance that can be controlled by the parameters N_g and N_h . The higher the noise, the lower the achievable spatial resolution for a given accuracy, so the level of optical scattering is important for high SNR, while not attenuating the signal and reducing penetration. Finally, we refer to the mean wavelength as the relative stiffness, neglecting viscoelasticity. This was motivated by the fact that in soft incompressible tissue, the elastic behaviour is dominated by the shear modulus that vary linearly with the square of the shear wave wavelength as commonly used in passive elastography³⁰. Our experimental data (Fig. 2c), showing strong linear dependency ($r = 0.994$) between measured Young's modulus and the square of the shear wave wavelength validated that viscoelastic behaviour could be neglected in this approximation. In our study, we have validated the approach using common examples where stiffness is a core assessment during culture or outcome assessment. Our results have shown how we can assess orthopaedic tissues such as cartilage and bone during differentiation in intact tissues, tissue engineered cancer models, fertility assessment of oocytes in vitro, and ophthalmological applications where assessment can be made of biomaterial stiffness with time following implantation.

Debiased ambient vibrations OCE is a powerful tool for spatially assessing biomaterials and biomatrices in vitro in 3D culture, as it produces a quantitative mechanical contrast image, or λ -map, that is decoupled from the standard scattering intensity

image from OCT, and this extra information can be used to indicate important changes in the specimen. Additionally, one can extract the 'relative stiffness' of a region as the mean squared wavelength, which will be directly proportional to the Young's modulus of an isotropic linearly elastic material, as validated in agarose samples. Using biological systems with varying matrix properties, we show that this effective and 'simple to use' approach offers a breakthrough in on-line tissue mechanical assessment of spatial mechanical properties for organoids, soft tissues and tissue engineering.

Methods

Measurement system and data processing. The system used for the agarose and hMSC pellet study was a Thorlabs Telesto-II spectral domain OCT system with central source wavelength 1310 nm equipped with a scan lens (LSM03 Thorlabs) resulting in an axial resolution of $4.1\mu\text{m}$ in tissue and a lateral resolution of 15 micrometre. The acquisition consisted of 192 frames, each with 1000 A-scans at a rate of 48 kHz. In the case of the oocyte and cancer seeded collagen gels, the system was a Wasatch Photonics 800 nm system with spectral bandwidth of 92 nm, with measurements consisting of 100 frames of 512 A-scans at a rate of 30 kHz. In all cases, the samples were placed in standard tissue culture well plates on the same bench as the OCT probe to allow transmission of vibrations.

Pre-processing was performed with bespoke software to: resample the spectrometer to k -space, remove the background signal and take the fast Fourier transform to map into complex valued delay space. The displacement fields between subsequent frames were then estimated with

$$d = \frac{\lambda_0}{4\pi n_{\text{eff}}} \text{atan}2(\Im\{p_i p_{i+1}^*\}, \Re\{p_i p_{i+1}^*\}), \quad (1)$$

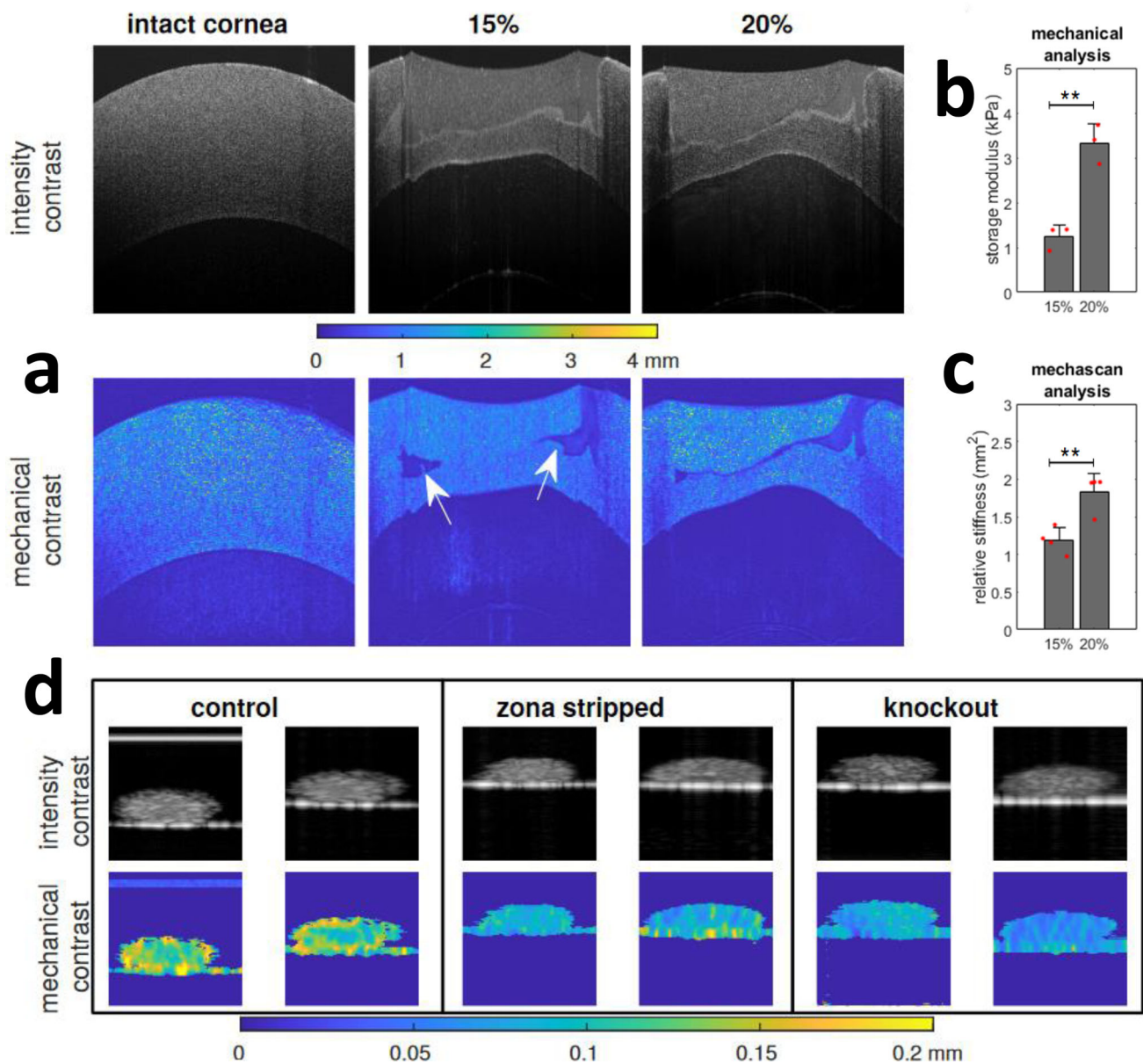


Fig. 5 debiased ambient vibration OCE applications to tissue samples. **a** Shows the intensity and mechanical contrast of porcine corneas intact and after implanting two different concentrations of hydrogel; the white arrows indicate areas of uncured gel, which show high mechanical contrast but not in intensity. **b** Shows storage modulus from rheology from samples of hydrogel ($n = 3$). **c** Shows relative stiffness from OCT scans ($n = 3$). **d** Shows a study on the mechanical properties of mouse oocytes: comparing zona intact and zona-free wild-type oocytes and intact histone H3.3 knockout oocytes; the zona intact wild type oocytes exhibit greater stiffness heterogeneity markedly different from zona-free and less developmentally competent zona-intact H3.3 knockout. Oocytes pictures have been cropped to 100×300 micrometres ($x-z$). * denotes a significant difference with a $p < 0.05$ and ** of $p < 0.01$ as calculated with 1-way Anova test followed by a Tukey-Kramer comparison of means. Error bars represent the standard deviation.

where λ_0 is the central wavelength of the source, n_{eff} is the effective refractive index of the sample, \Re and \Im take the real and imaginary parts, and p_{t+1} is the subsequent complex measurement from p_t . From these displacement fields, the elastic wavelengths are then estimated through ().

Estimating stiffness from noiseless asynchronous time frames. We wish to estimate the spatially resolved stiffness of a material through its wave speed given as

$$v = \sqrt{\frac{M}{\rho}}, \quad (2)$$

where ρ is its mass density and M is some elastic modulus factor. This generic form applies to: shear waves, where $M = \frac{1}{3}\mu$, with μ the shear modulus; P-waves, where $M = K + \frac{4}{3}\mu$, with K the bulk modulus; and Rayleigh surface waves, where $M = \frac{(0.862+1.14\nu)^2}{2(1+\nu)^2}\mu$ with ν the Poisson's ratio. As with any travelling wave, the velocity can

be expressed as $v = \lambda f$, where λ is its spatial wavelength, and f its temporal frequency. If f and ρ are either known or known to be fixed a priori, then one can calculate the elastic modulus M directly from measured λ .

Assuming shear waves, as in refs. [29,31], and a linearly elastic isotropic material, the Young's modulus can be found as

$$E = 2(1 + \nu)\rho f^2 \lambda^2 \quad (3)$$

Given periodic elastic waves propagating through a heterogeneous material, one can measure its displacement at a position x as

$$d_x(t) = a \sin\left(\frac{2\pi x}{\lambda} + \phi(t)\right), \quad (4)$$

where a is the amplitude of the wave, λ is the spatial wavelength and $\phi(t)$ is a phase function describing the position of the wave at time, t . One can also estimate the

local strain as a finite difference approximation to a derivative as

$$s_x(t) = \frac{2\pi a}{\lambda} \cos\left(\frac{2\pi x}{\lambda} + \phi(t)\right) \approx \frac{d_{x+1}(t) - d_{x-1}(t)}{2\Delta x}, \quad (5)$$

where Δx is the resolution of the imaging system. Given that the energy of a sufficiently sampled sinusoid is $N_t a^2/2$ regardless of the order of samples, it follows that λ can be found through

$$\lambda = 2\pi \sqrt{\frac{\sum_{t=1}^{N_t} d(t)^2}{\sum_{t=1}^{N_t} s(t)^2}}, \quad (6)$$

where $\sum_{t=1}^{N_t} d(t)^2$ is the displacement energy from a sequence of wave measurements as represented in Eq. (4). The estimate in Eq. (6) is equivalent to that presented in ref. ²⁹ and used in ref. ³⁰. The estimate in Eq. (6) is exact in a noiseless system as $\Delta x \rightarrow 0$ and the number of temporal samples $N_t \rightarrow \infty$. In this case, $\phi(t)$ can take the form $\phi(t) = kt$, where k is a scalar, or a random function spanning $[-\pi, \pi]$ with uniform probability density. For example, if one has linear sampling with timing jitter such as $\phi(t) = kt + n$ with $n \sim \mathcal{N}(0, \sigma_n^2)$, then Eq. (6) is still accurate for sufficiently many measurements.

Robust estimation with noise. Although the wavelength estimation in Eq. (6) holds in the noiseless case, it is heavily biased by any phase noise in practice. This is because the shear wavelength is in the millimetre range^{29,31}, which is far greater than the spatial sampling resolution in OCT, so any additive wide band noise will be amplified by the gradient in Eq. (5).

For additive white Gaussian noise (AWGN), $n \sim \mathcal{N}(0, \sigma^2)$, with variance σ^2 , the signal energy after filtering with some kernel h is

$$E_n = \sigma^2 \sum_{k=1}^{N_h} h_k^2, \quad (7)$$

where N_h is the length of h . For example, the central difference gradient approximation in Eq. (5) is equivalent to spatially filtering the displacement vector with kernel $h = [-0.5, 0, 0.5]/\Delta x$, which has an energy of $E_n = 0.5\sigma^2/\Delta x^2$. If σ can be estimated from the samples, then one can form the debiased estimate of wavelength as

$$\lambda = 2\pi \sqrt{\frac{\sum_{t=1}^{N_t} d(t)^2 - N_t \sigma^2}{\sum_{t=1}^{N_t} (h * d(t))^2 - \sigma^2 \sum_{k=1}^{N_h} h_k^2}}, \quad (8)$$

where $*$ denotes spatial convolution.

While Eq. (8) may be reasonable in moderately low noise, when the noise energies are similar to the signal energies, it will produce high variance or even undefined estimates. This can be compensated to some degree by increasing N_g or N_h , but at the expense of temporal response rate and scan time or spatial resolution in the gradient direction and will not control the numerator going negative. We therefore introduce an additional 2D low-pass filter to the displacement vectors. This debiased filtered estimate as

$$\lambda = 2\pi \sqrt{\frac{\sum_{t=1}^{N_t} (g * d(t))^2 - \sigma^2 \sum_{k=1}^{N_g} g_k^2}{\sum_{t=1}^{N_t} (h * g * d(t))^2 - \sigma^2 \sum_{k=1}^{N_{hg}} (h * g)_k^2}}, \quad (9)$$

where g is the 2D low-pass filter, and $N_{hg} = N_h + N_g - 1$ is the length of the effective strain filter kernel. We use a 2D Gaussian function for g since it will not introduce any ripple artifacts, with size $N_g = [2c_g] + 1$, where c_g is its spatial standard deviation of the Gaussian. The Gaussian filter generated a speckle pattern on the mechanical contrast maps.

Despite the filtering and effective noise power reduction in Eq. (9), there still may be cases of undefined estimates due to potential negativity. To avoid this, we adopt a ‘soft subtraction’ approach as used in X-ray computed tomography scatter correction³⁹

$$S(a - b) = a(1 - \gamma), \quad (10)$$

which replaces the operation $a - b$, where γ is a compensation factor that can be calculated as

$$\gamma = \begin{cases} \beta & \text{if } b \geq \beta a \\ \frac{b}{a} & \text{otherwise,} \end{cases} \quad (11)$$

where $\beta = [0, 1]$ is a thresholding term that we set to $\beta = 0.9$ in this work. In our experiments, this only starts to contribute very deep in the samples, where the intensity is too low for a reliable measurement anyway.

One last consideration for this method is determining the noise variance σ^2 . Under the assumptions this is space varying and the wavelength is significantly larger than the spatial resolution of the OCT system, it can be approximated as the time-averaged variance within a sliding 3×3 window.

Agarose gel study. In all, 1%, 2% and 3% agarose hydrogels containing 1% milk were fabricated in this study. Briefly, Type I agarose (Fisher scientific, UK) was added to distilled water and autoclaved at 121 °C to make 2%, 4% and 6% agarose solutions. 2% milk solution was prepared by dissolving nonfat dry milk powder (Bio-rad, UK) in distilled water and this solution was mixed with equal volume of

2%, 4% and 6% agarose solution at 100 °C and cast into a dish and allowed to solidify at room temperature to produce 1%, 2% and 3% agarose gels containing 1% milk. 2/3% hybrid gels were made by scraping part of 2% gel and adding 3% agarose solution into the dish and allowed to solidify. Gels were then cored using a biopsy punch to produce discs of 6 mm in diameter and 2 mm in thickness. These gels were then placed into a 96-well tissue culture plate with 100 µL distilled water covering the surface of each gel and imaged with OCT for wavelength measurement as described earlier.

The Young’s modulus of these agarose gels were tested using Bose ElectroForce 5500 (TA Instruments, UK). Briefly, excessive water was removed from agarose gels and a preload of 0.01 N was used to ensure direct contact between sample and plate surfaces. An unconfined ramp compression (up to 10% strain of the sample thickness) was performed and the Young’s modulus was calculated from the stress-strain curve.

Chondrogenic and osteogenic cell pellet study. Sheep hind leg was purchased from a local abattoir and ovine mesenchymal stem cells (MSCs) were isolated from the bone marrow of the femur. Thus, no ethical approval was needed for this study. MSCs from passage two were trypsinised and 200,000 cells were added into each well of a v-bottomed 96-well plate (Greiner bio-one) and centrifuged for 5 min at 500 × g to form cell pellets.

For chondrogenic differentiation, cell pellets were cultured in a differentiation medium consisting of high glucose DMEM supplemented with 2 mM L-glutamine, 100 U/mL penicillin-0.1 mg/mL streptomycin, 100 µg/mL sodium pyruvate, 40 µg/mL L-proline, 50 µg/mL L-ascorbic acid-2-phosphate, 4.7 µg/mL linoleic acid, 1.5 mg/mL bovine serum albumin (BSA), 1 × insulin-transferrin-selenium, 100nM dexamethasone (all from Sigma-Aldrich, UK) and 10 ng/mL recombinant Human TGF-β3 (Peprotech, UK) for 3 weeks, with medium being exchanged three times a week. During this differentiation period, half of pellets were subjected to hydrostatic pressure (HP, 270 kPa, 1Hz, 1 h/day) to enhance the differentiation, whereas the rest were not stimulated and kept as control. Both control and HP groups were harvested at end of differentiation period and imaged with OCT for wavelength measurement. Samples were then digested with papain for measurement of their glycosaminoglycan (GAG) content using dimethylmethylen blue dye-binding assay. Samples were also harvested for histology, wax embedded, sectioned and stained with 1% alcian blue 8GX in 0.1 M HCl for GAG distribution.

For osteogenic differentiation, cell pellets were cultured in a differentiation medium consisting of low glucose DMEM supplemented with 10% fetal bovine serum, 2 mM L-glutamine, 100 U/mL penicillin-0.1 mg/ml streptomycin, 100 nM dexamethasone, 50 µM L-ascorbic acid-2-phosphate and 10 mM β-glycerophosphate (all Sigma-Aldrich, UK) for 3 weeks, with medium being exchanged three times a week. During this differentiation period, samples were continuously monitored using OCT in a sterile manner for wavelength measurement at days 3, 10 and 21, with separate samples in parallel culture being terminated for mechanical testing and histology at same time points. The Young’s modulus of osteogenic cell pellets were tested using a customised rig designed for testing microspheres and cell organoids⁴⁰. After excessive water was removed, cell pellets were plated between two platen surfaces and an unconfined ramp compression (up to 25% strain of the sample diameter) was performed and the Young’s modulus was calculated from the stress-strain curve. For histological analysis, cell pellets were embedded in wax, sectioned and stained with picrosirius red for collagen accumulation.

Collagen study. Collagen/fibroblast matrices were created using the methodology outlined in Timpson et al.⁴¹. The matrices were incubated at 37 °C, 5% CO₂ for 15 days to allow the collagen/fibroblast matrix to contract. The collagen/fibroblast matrix was imaged using OCT on days 1, 4, 7, 11 and 15 of the sample contraction.

Using the protocol outlined in Hallas-Potts et al.⁴², one collagen/fibroblast matrix with A2780 cultured on top and one blank collagen/fibroblast matrix with no cells cultured on top were prepared and transferred to a metal grid. Moving the collagen matrix to the grid is referred to day 0. Dishes were incubated at 37 °C with 5% CO₂ for 7 days to allow the cells to invade. The collagen/fibroblast matrices were imaged on days 2 and 7.

Immediately after OCT imaging, the matrix was removed from the grid and added to a falcon tube with 5 mL 4% (w/v) paraformaldehyde (PFA) to fix overnight. The fixed collagen/fibroblast matrix was embedded in wax, sectioned and stained with haematoxylin and eosin (H&E) by the CRUK Edinburgh Centre Pathology & Phenomics Lab. Stained sections were imaged on the Nanoozoomer XR model, data captured using NDP scan v 3.1. ×40 magnification.

Corneal study. Freshly enucleated porcine eyes were purchased from the local butcher. To induce corneal injury, a 5 mm biopsy punch was used to make a partial cut in the central cornea to a depth of approximately 50%. Then, a solution of methacrylated silk fibroin (15 or 20 wt%) containing 0.5% (w/v) lithium phenyl-2,4,6-trimethylbenzoylphosphonate (LAP) was filled to the defect and photo-crosslinked for 5 min (365 nm, 3 mW/cm²). Fresh corneal, injured corneal and silk fibroin hydrogel repaired corneal was then imaged with OCT for wavelength measurement as described earlier. The storage modulus (G) of freshly prepared Silk-MA hydrogels were measured in oscillatory mode at 32 °C using a plate-plate geometry (Kinexus Pro+, Malvern, UK). After running an amplitude sweep to

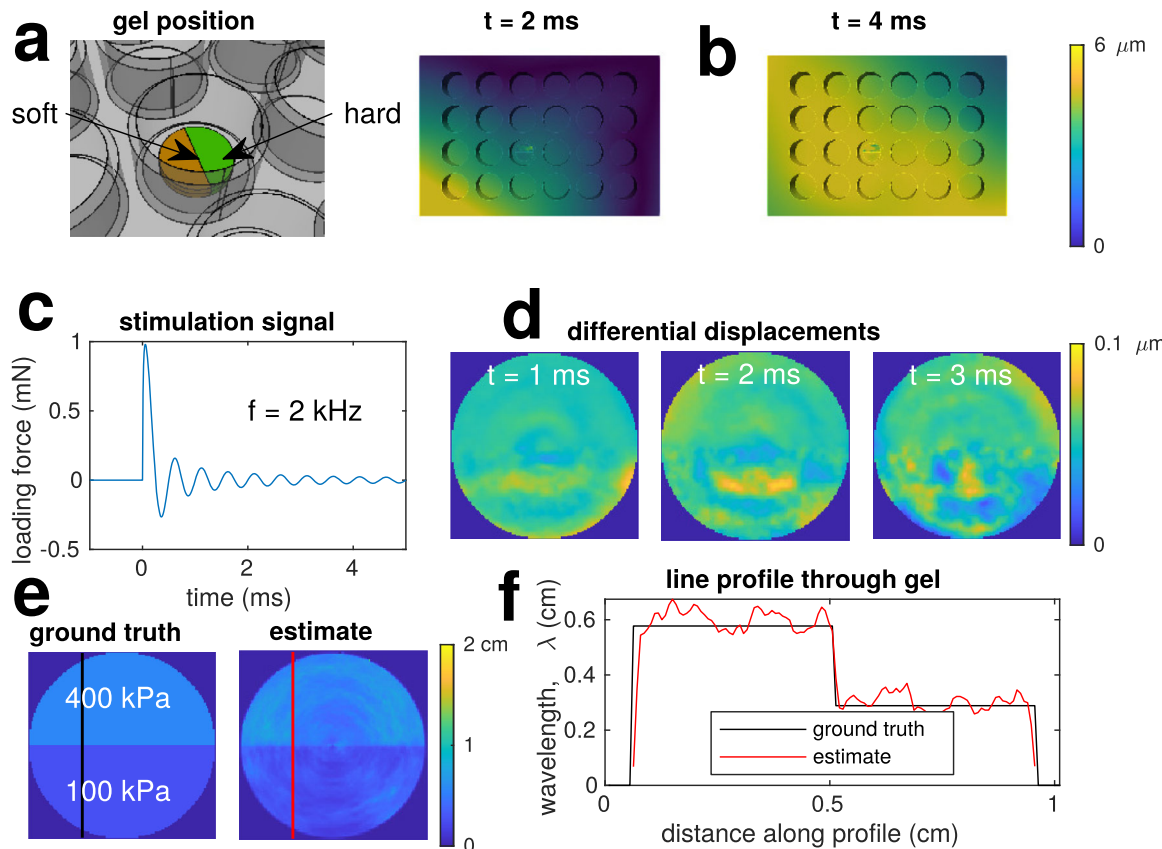


Fig. 6 FEM simulation of vibrating multi-well plate with heterogeneous gel. **a** Shows the gel seated on the base on a well. **b** Shows the displacement magnitudes of the plate at $t = 2\text{ ms}$ and $t = 4\text{ ms}$. **c** Shows the excitation force applied to a corner of the plate: a 2 kHz sinusoid with exponentially decaying amplitude. **d** Shows examples of the differential displacements in the axial direction at the centre of the gel. **e** Shows the estimated wavelength over the gel surface and the ground truth assuming shear waves of 2 kHz. Panel **f** are profile plots are the lines indicated in **e**.

determine the linear viscoelastic range (LVER), a frequency sweep was conducted at 0.5% shear strain. The experiments were conducted in triplicate.

Finite element method simulation of vibrational elastography. To demonstrate the concept of vibrational elastography, a set of FEM simulations were run, as summarised in Fig. 6. This was performed with code_aster⁴³ on a mesh containing a 24-well polystyrene plate and heterogeneous gel with a dynamic load applied axially to one corner of the plate. There were 36,000 nodes at the central plane of the gel with thickness 2 mm and diameter 10 mm, whose positions were sampled every 10 μs over a total simulation time of 5 ms. The loading signal used for stimulation was $\sin(2\pi ft)/t$, where $f = 2\text{ kHz}$, with the opposite corner fixed as a boundary condition—other combinations of loads were also tested with similar resulting displacement fields and estimates.

The wavelengths of any resulting elastic waves in this noiseless case were estimated using Eq. (6). Firstly, the axial positions at each time instance were resampled onto a polar grid with origin at the centre of the gel so that the strains were estimated along effective cross-sections as used in the experimental section. The estimate from Eq. (6) was applied to the 400 displacement (differential position) fields between $t = [1, 4]\text{ ms}$. Finally, these wavelengths were resampled onto a Cartesian grid to form an image.

Determining spatial resolution. We use a Blonski⁴⁴ edge method variant also adopted by ref. ³¹ for the spatial resolution: first fitting the sigmoid function

$$f = \frac{L}{1 + e^{-k(x-x_0)}} + C, \quad (12)$$

with the Levenberg–Marquardt algorithm for the parameters (L, k, x_0, C) then finding the full-width at half-maximum (FWHM) of the sigmoid derivative, which can be expressed as

$$\text{FWHM}(f') = \frac{2}{k} \log(3 + \sqrt{2}). \quad (13)$$

Statistics and reproducibility. We used a one-way ANOVA followed by a Tukey–Kramer test in Matlab (The Mathworks) to test for significant differences with p values <0.01 or <0.05 and a number of samples $N > 3$.

Reporting summary. Further information on research design is available in the Nature Portfolio Reporting Summary linked to this article.

Data availability

The optical coherence tomography datasets generated during and/or analysed during the current study are available from the corresponding author on reasonable request. The measurements dataset behind the bargraphs can be found on figshare. <https://doi.org/10.6084/m9.figshare.22148093.v3>.

Code availability

The matlab codes to implement the algorithms described in this paper are available from the corresponding author on reasonable request.

Received: 13 September 2021; Accepted: 31 March 2023;

Published online: 18 May 2023

References

- Guimarães, C. F., Gasperini, L., Marques, A. P. & Reis, R. L. The stiffness of living tissues and its implications for tissue engineering. *Nat. Rev. Mater.* **5**, 351–370 (2020).
- Wall, M. et al. Key developments that impacted the field of mechanobiology and mechanotransduction. *J. Orthop. Res.* **36**, 605–619 (2018).
- Mullender, M. et al. Mechanotransduction of bone cells in vitro: mechanobiology of bone tissue. *Med. Biol. Eng. Comput.* **42**, 14–21 (2004).
- Klein, T. J., Malda, J., Sah, R. L. & Hutmacher, D. W. Tissue engineering of articular cartilage with biomimetic zones. *Tissue Eng. B Rev.* **15**, 143–157 (2009).
- Khoshgoftaar, M., Wilson, W., Ito, K. & van Donkelaar, C. C. The effect of tissue-engineered cartilage biomechanical and biochemical properties on its

- post-implantation mechanical behavior. *Biomechan. Model. Mechanobiol.* **12**, 43–54 (2013).
6. Baas, E., Kuiper, J. H., Yang, Y., Wood, M. A. & El Haj, A. J. In vitro bone growth responds to local mechanical strain in three-dimensional polymer scaffolds. *J. Biomechan.* **43**, 733–739 (2010).
 7. Luo, L., Chu, J. Y. J., Eswaramoorthy, R., Mulhall, K. J. & Kelly, D. J. Engineering tissues that mimic the zonal nature of articular cartilage using decellularized cartilage explants seeded with adult stem cells. *ACS Biomater. Sci. Eng.* **3**, 1933–1943 (2017).
 8. Luo, L., Thorpe, S. D., Buckley, C. T. & Kelly, D. J. The effects of dynamic compression on the development of cartilage grafts engineered using bone marrow and infrapatellar fat pad derived stem cells. *Biomed. Mater.* **10**, 055011 (2015).
 9. Luo, L., O'Reilly, A. R., Thorpe, S. D., Buckley, C. T. & Kelly, D. J. Engineering zonal cartilaginous tissue by modulating oxygen levels and mechanical cues through the depth of infrapatellar fat pad stem cell laden hydrogels. *J. Tissue Eng. Regen. Med.* **11**, 2613–2628 (2017).
 10. Suresh, S. Elastic clues in cancer detection. *Nat. Nanotechnol.* **2**, 748–749 (2007).
 11. Xu, X., Farach-Carson, M. C. & Jia, X. Three-dimensional in vitro tumor models for cancer research and drug evaluation. *Biotechnol. Adv.* **32**, 1256–1268 (2014).
 12. Xu, M., Lerner, A. L., Funkenbusch, P. D., Richhariya, A. & Yoon, G. Sensitivity of corneal biomechanical and optical behavior to material parameters using design of experiments method. *Comput. Methods Biomechan. Biomed. Eng.* **21**, 287–296 (2018).
 13. Nguyen, B. V. et al. Biomechanical properties of single chondrocytes and chondrons determined by micromanipulation and finite-element modelling. *J. R. Soc. Interface* **7**, 1723–1733 (2010).
 14. Nguyen, B. V. et al. Strain-dependent viscoelastic behaviour and rupture force of single chondrocytes and chondrons under compression. *Biotechnol. Lett.* **31**, 803–809 (2009).
 15. Krouskop, T. A., Dougherty, D. R. & Vinson, F. S. A pulsed Doppler ultrasonic system for making noninvasive measurements of the mechanical properties of soft tissue. *J. Rehabil. Res. Dev.* **24**, 1–8 (1987).
 16. Muthupillai, R. et al. Magnetic resonance elastography by direct visualization of propagating acoustic strain waves. *Science* **269**, 1854–1857 (1995).
 17. Kennedy, B. F., Wijesinghe, P. & Sampson, D. D. The emergence of optical elastography in biomedicine. *Nat. Photon.* **11**, 215–221 (2017).
 18. Fujimoto, J. G., Pitriss, C., Boppart, S. A. & Brezinski, M. E. Optical coherence tomography: an emerging technology for biomedical imaging and optical biopsy. *Neoplasia* **2**, 9–25 (2000).
 19. Wojtkowski, M. et al. Ultrahigh-resolution, high-speed, Fourier domain optical coherence tomography and methods for dispersion compensation. *Optics Express* **12**, 2404–2422 (2004).
 20. Zvyagin, A. V., Smith, E. D. J. & Sampson, D. D. Delay and dispersion characteristics of a frequency-domain optical delay line for scanning interferometry. *J. Opt. Soc. Am. A* **20**, 333 (2003).
 21. Rogowska, J. Optical coherence tomographic elastography technique for measuring deformation and strain of atherosclerotic tissues. *Heart* **90**, 556–562 (2004).
 22. Chan, R. et al. OCT-based arterial elastography: robust estimation exploiting tissue biomechanics. *Optics Express* **12**, 4558 (2004).
 23. Wang, R. K., Kirkpatrick, S. & Hinds, M. Phase-sensitive optical coherence elastography for mapping tissue microstrains in real time. *Appl. Phys. Lett.* **90**, 164105 (2007).
 24. Larin, K. V. & Sampson, D. D. Optical coherence elastography - OCT at work in tissue biomechanics [Invited]. *Biomed. Optics Express* **8**, 1172–1202 (2017).
 25. Wang, S. & Larin, K. V. Shear wave imaging optical coherence tomography (SWI-OCT) for ocular tissue biomechanics. *Optics Lett.* **39**, 41 (2014).
 26. Rajput, S. & Thakur, N. K. In *Geological Controls for Gas Hydrate Formations and Unconventionals* 131–164 (Elsevier, 2016).
 27. Ramier, A. et al. In vivo measurement of shear modulus of the human cornea using optical coherence elastography. *Sci. Rep.* **10**, 17366 (2020).
 28. Gallot, T. et al. Passive elastography: shear-wave tomography from physiological-noise correlation in soft tissues. *IEEE Trans. Ultrasonics, Ferroelectrics Frequency Control* **58**, 1122–1126 (2011).
 29. Catheline, S. et al. Tomography from diffuse waves: passive shear wave imaging using low frame rate scanners. *Appl. Phys. Lett.* **103**, 014101 (2013).
 30. Nguyen, T.-M. et al. Diffuse shear wave imaging: toward passive elastography using low-frame rate spectral-domain optical coherence tomography. *J. Biomed. Optics* **21**, 126013 (2016).
 31. Zvietcovich, F., Pongchalee, P., Meemon, P., Rolland, J. P. & Parker, K. J. Reverberant 3D optical coherence elastography maps the elasticity of individual corneal layers. *Nat. Commun.* **10**, 4895 (2019).
 32. Hyle Park, B. et al. Real-time fiber-based multi-functional spectral-domain optical coherence tomography at 13 μm . *Optics Express* **13**, 3931 (2005).
 33. Kennedy, B. F. et al. Strain estimation in phase-sensitive optical coherence elastography. *Biomed. Optics Express* **3**, 1865 (2012).
 34. Hochmuth, R. M. Micropipette aspiration of living cells. *J. Biomechan.* **33**, 15–22 (2000).
 35. Yanez, L. Z., Han, J., Behr, B. B., Pera, R. A. R. & Camarillo, D. B. Human oocyte developmental potential is predicted by mechanical properties within hours after fertilization. *Nat. Commun.* **7**, 10809 (2016).
 36. Wen, D. et al. Histone variant H3.3 is an essential maternal factor for oocyte reprogramming. *Proc. Natl Acad. Sci. USA* **111**, 7325–7330 (2014).
 37. Grasland-Mongrain, P. et al. Ultrafast imaging of cell elasticity with optical microelastography. *Proc. Natl Acad. Sci. USA* **115**, 861–866 (2018).
 38. Sabra, K. G., Conti, S., Roux, P. & Kuperman, W. A. Passive in vivo elastography from skeletal muscle noise. *Appl. Phys. Lett.* **90**, 194101 (2007).
 39. Sun, M. & Star-Lack, J. M. Improved scatter correction using adaptive scatter kernel superposition. *Phys. Med. Biol.* **55**, 6695–6720 (2010).
 40. Yan, Y. et al. Mechanical characterization of agarose micro-particles with a narrow size distribution. *Powder Technol.* **192**, 122–130 (2009).
 41. Timpson, P. et al. Organotypic collagen I assay: a malleable platform to assess cell behaviour in a 3-dimensional context. *J. Vis. Exp.* <http://www.jove.com/details.php?id=3089> (2011).
 42. Hallas-Potts, A., Dawson, J. C. & Herrington, C. S. Ovarian cancer cell lines derived from non-serous carcinomas migrate and invade more aggressively than those derived from high-grade serous carcinomas. *Sci. Rep.* **9**, 5515 (2019).
 43. Electricité de France. Finite element code_aster, analysis of structures and thermomechanics for studies and research. Open source on www.code-aster.org (2019).
 44. Blonski, S., Pagnutti, M. A., Ryan, R. & Zanoni, V. In-flight edge response measurements for high-spatial-resolution remote sensing systems. *Proc. SPIE* **4814**, 317–326 (2002).

Acknowledgements

We would like to acknowledge the support from an ERC Advanced award to A.J.EH; 638836: H2020_ERC_DYNACEUTICS and the MRC UKRMP Hub Engineering the Cell Environment.

Author contributions

J.H.M., L.L., Y.R., Y.Y., S.W., A.J.E.H. and P.B. designed the study, the experiments and wrote the paper. J.H.M. wrote the algorithm. J.H.M. and L.L. acquired OCT scans. J.H.M., L.L., Y.R., M.F., A.H.P., V.S., C.J.L., I.A.B., Z.Z. and A.K.G. performed the experiments. J.H.M., L.L., C.S.H., A.J.E.H. and P.B. analysed the data.

Competing interests

The authors declare no competing interests.

Additional information

Supplementary information The online version contains supplementary material available at <https://doi.org/10.1038/s42003-023-04788-0>.

Correspondence and requests for materials should be addressed to Alicia J. El Haj or Pierre O. Bagnaninchi.

Peer review information Communications Biology thanks Stefan Catheline and the other, anonymous, reviewer(s) for their contribution to the peer review of this work. Primary handling editors: Alexander Cartagena-Rivera, Anam Akhtar, and Christina Karlsson Rosenthal.

Reprints and permission information is available at <http://www.nature.com/reprints>

Publisher's note Springer Nature remains neutral with regard to jurisdictional claims in published maps and institutional affiliations.



Open Access This article is licensed under a Creative Commons Attribution 4.0 International License, which permits use, sharing, adaptation, distribution and reproduction in any medium or format, as long as you give appropriate credit to the original author(s) and the source, provide a link to the Creative Commons license, and indicate if changes were made. The images or other third party material in this article are included in the article's Creative Commons license, unless indicated otherwise in a credit line to the material. If material is not included in the article's Creative Commons license and your intended use is not permitted by statutory regulation or exceeds the permitted use, you will need to obtain permission directly from the copyright holder. To view a copy of this license, visit <http://creativecommons.org/licenses/by/4.0/>.